$Na_4MnV(PO_4)_3$-rGO as Advanced Cathode for Aqueous and Non-Aqueous Sodium Ion Batteries

*P. Ramesh Kumar, Aziz Kheireddine, Umair Nisar, R. A. Shakoor, Rachid Essehli, Ruhul Amin * and Ilias Belharouak **

Dr. P. Ramesh Kumar, Dr. Aziz Kheireddine, Dr. Rachid Essehli, Dr. Ruhul Amin
Qatar Environment and Energy Research Institute (QEERI), Hamad Bin Khalifa University, Qatar Foundation, Doha, Qatar.
E-mail: mdruhul@hbku.edu.qa

Umair Nisar, Dr. R. A. Shakoor
Center for Advanced Materials (CAM), Qatar University, Doha, Qatar.

Dr. Ilias Belharouak
Energy and Transportation Science Division, Oak Ridge National Laboratory, Oak Ridge, TN, USA.
E-mail: belharouaki@ornl.gov

Keywords: Sodium ion batteries, aqueous batteries, NASICON, aqueous electrolyte, Energy storage, Grid.

Abstract

NASICON-type $Na_4MnV(PO_4)_3$ with reduced graphene oxide (rGO) has been synthesized by the simple sol-gel reaction and characterized by different analytical techniques. The resulted material has been explored as a cathode material for rechargeable non-aqueous and aqueous sodium-ion batteries. In non-aqueous electrolytes, the as-synthesized $Na_4MnV(PO_4)_3$-rGO composite shows stable discharge capacity of 86 mAh g^{-1} at 0.1 C and 68 mAh g^{-1} at 0.2 C after 100 cycles in half-cell and full-cell configurations, respectively. In aqueous electrolytes, it delivers an initial discharge capacity of 92 mAh g^{-1} at 1 C rate in half-cells and 97 mAh g^{-1} at 10 C rate in full-cells having $NaTi_2(PO_4)_3$-MWCNT as the anode. Stable cycleability and high rate capabilities of $Na_4MnV(PO_4)_3$-rGO composite can be attributed to the very strong and sustainable conductive percolation networks for both electrons and Na^+ ions. The obtained results reveal that the aqueous electrolyte cell has a huge scope for gird level energy storage applications.

1. Introduction

The rationales for researching and developing sodium-ion batteries (SIBs) are the everlasting availability of sodium, the compelling similarity in science and engineering between SIBs and Li-ion batteries, and the prospect of applying the Na-ion battery technology as stationary energy storage systems for on- and off-grid storage applications.[1] To date, various transition metal oxides such as Na_xCoO_2, Na_xCrO_2,[2] Na_xMnO_2,[3] P_2-$Na_x[Fe_{1/2}Mn_{1/2}]O_2$,[4] and O_3-$Na[Ni_{1/3}Fe_{1/3}Mn_{1/3}]O_2$; and polyanionic compounds such as $NaFePO_4$,[5] $Na_3V_2(PO_4)_3$, $NaFe_2(PO_4)_2(SO_4)_2$,[6] Na_2FePO_4F, $Na_{1.86}\square_{0.14}Fe_3(PO_4)_3$,[7] $Na_3V_2(PO_4)_2F_3$ and $Na_3V_2O_2(PO_4)_2F$,[8] had been reported as cathodes for SIBs.[9] Among these compounds, $Na_3V_2(PO_4)_3$ is of peculiar interest owing to the NASICON framework that favors the reversible removal/uptake of Na-ions over the voltage plateau of 3.3−3.4 V. This voltage is associated with the electrochemical activity of the redox couple V^{4+}/V^{3+} and leads to the generation of a specific theoretical capacity of 110 mAh g^{-1}.[10] Recently, Zhou et al. replaced half of vanadium in $Na_3V_2(PO_4)_3$ with other elements to make $Na_4VM(PO_4)_3$ (M = Fe, Mn & Ni) without jeopardizing the NASICON crystalline arrangement. Of significance, $Na_4VMn(PO_4)_3$ has shown advantages in terms of electrochemical performance compared to the other materials, and has to the promise to be an inexpensive cathode candidate. Indeed, $Na_4VMn(PO_4)_3$ exhibited a relatively higher specific capacity (110 mAh g^{-1}) due to the reaction of up to two Na-ions per unit formula of $Na_4VMn(PO_4)_3$, and the simultaneous electrochemical activation of V^{4+}/V^{3+} and Mn^{3+}/Mn^{2+} at 3.3 and 3.6 V, respectively.[11] The drawback, however, is that $Na_4MnV(PO_4)_3$ is a poor electronic conductor.[12] Nonetheless, Li et al. improved the electronic conductivity of $Na_4MnV(PO_4)_3$ in combination with graphene aerogel by means of sol-gel synthesis.[13] The graphene-based composite achieved an energy density of 380 Wh kg^{-1} at the 0.5 C rate, and retained 69 % of its initial capacity after completion of 4000 cycles at 20 C in the presence of non-aqueous electrolytes.[13] Despite these improvements, three major hurdles have to be overcome before the implementation of

sodium ion batteries in large scale can happen: 1) most of the sodium-based cathodes are much more moisture sensitive compared to their lithium-based counterparts; this implies that the handling, processing and fabrication of electrodes and cells need extra care, and hence, a cost penalty is unavoidable, 2) if no rigorous dry conditions are applied, the use of non-aqueous electrolytes will likely trigger undesired chemical and electrochemical reactions, and hence, a performance penalty is compulsory, and 3) even if handling and processing are well mitigated, the use of non-aqueous electrolytes comes with a cost disadvantage and remains a problem because of the possibility of thermal runaway.[14] In stationary SIBs battery applications where energy density is not the primary barrier, the value proposition could be further reinforced by virtue of use of aqueous electrolytes where the advantages of non-flammability, fast ion mobility and lower manufacturing cost would be most suitable for grid level storage systems.[15] Indeed, recent works dealt with alkaline metal-ion aqueous batteries using electrode materials ,[16] such as, LiV_3O_8,[17] TiP_2O_7,[18] $LiTi_2(PO_4)_3$,[19] $Na_3Ti_2(PO_4)_3$,[20] $Na_{0.44}MnO_2$,[21] $Na_2NiFe(CN)_6$, $Na_2CuFe(CN)_6$, $Na_{0.95}MnO_2$[22] and $Na_3V_2O_{2X}(PO_4)_2F_{3-2x}$[23]. The caveat is the poor cycle life that has been observed in the majority of the aqueous rechargeable alkali-metal ion batteries due to side reactions.[24]

The present work reports on the electrochemical performance of the composite $Na_4MnV(PO_4)_3$-rGO using both aqueous and non-aqueous electrolytes. $Na_4MnV(PO_4)_3$-rGO with reduced graphene was synthesized by the sol-gel method. The electrochemical performances of the composite cathode are compared in terms of specific capacity, cycle life and rate capability. The overall study embodies the first report on the electrochemical stability of $Na_4MnV(PO_4)_3$-rGO in the presence of aqueous electrolytes, where we shed the light on the potential use of this material in rechargeable aqueous SIBs for grid storage applications.

2. Results and Discussion

2.1. Structural and microstructural characterization

Powder x-ray pattern of the composite $Na_4MnV(PO_4)_3$-rGO compared to a reference is shown in **figure 1**. The indexation confirms that the material belongs to the trigonal (R-3c) space group with the lattice parameters a = 8.96354(2) Å and c = 21.48319(7) Å, and the unit cell volume V = 1494.82(1) $Å^3$, which is in agreement with previous reports.[25] The crystalline structure of $Na_4MnV(PO_4)_3$ is made of Mn/VO_6 octahedra and PO_4 tetrahedra that share corners, and hence form the anionic framework $[MnV(PO_4)_3]_4^-$. There exists two fully occupied and independent sodium sites surrounded by different oxygen environments (i.e. six-fold coordination for Na(1) (6b) site, and eight-fold coordination for Na(2) (18e) site).[25]

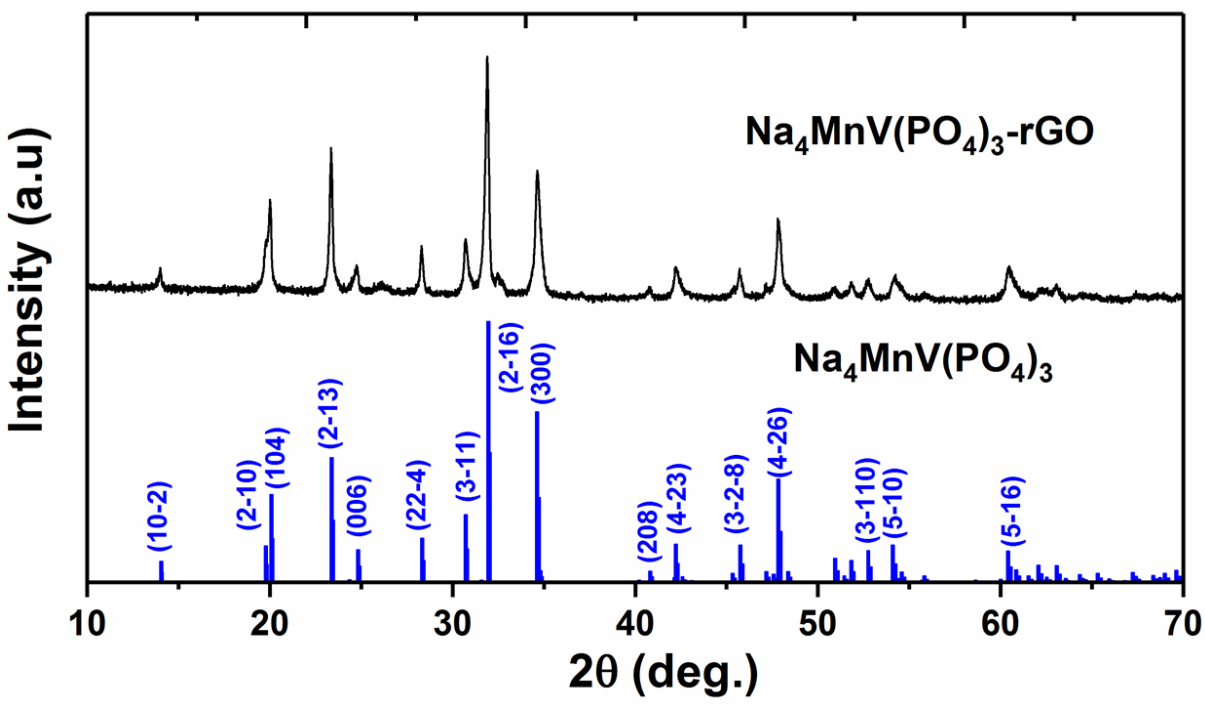

Figure 1: XRD patterns for $Na_4MnV(PO_4)_3$-rGO composite along with reference.

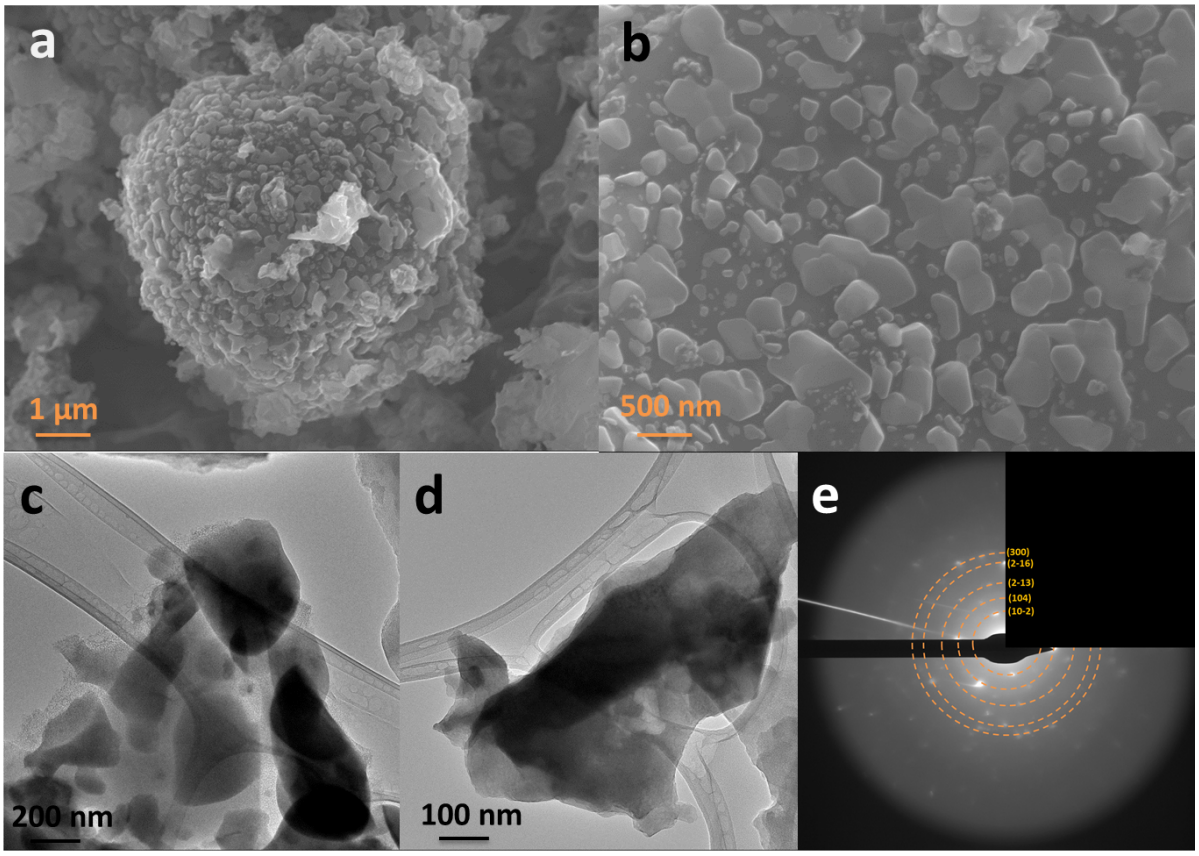

Figure 2: a, b) SEM images of $Na_4MnV(PO_4)_3$-rGO composite at different magnifications; c, d) TEM images and e) SAED patterns for the $Na_4MnV(PO_4)_3$-rGO composite.

Figure 2 shows the SEM and TEM images with different magnifications. The microstructure reveals that rGO is uniformly distributed across the interconnected particles of $Na_4MnV(PO_4)_3$ (cf. **figures 2a & b**), which would help improve the electronic conductivity of the composite cathode. The primary particle average sizes of $Na_4MnV(PO_4)_3$ are in the range of 300-500 nm. **Figure 2c & d** show TEM images that illustrate the integration between rGO and $Na_4MnV(PO_4)_3$ in the composite. The carbon weight percentage in the composite was 14 wt.% as determined by thermal gravimetric (TG) analysis (**Figure S1**). **Figure 2e** displays the observed Debye-Scherrer rings that represent the (10-2), (104), (2-13), (2-16), and (300) lattice planes, which matches well the crystalline structure of $Na_4MnV(PO_4)_3$. Elemental mapping obtained using energy-dispersive x-ray spectroscopy (EDX) on a single particle of $Na_4MnV(PO_4)_3$ is presented in **figure S2**. The EDX maps consistently confirm the presence

of sodium, vanadium, manganese, phosphorous, oxygen and carbon in the composite particle, and provides the evidence for the presence of rGO on top of the elemental purity of $Na_4MnV(PO_4)_3$. Overall, the results obtained by XRD, SEM, and TEM-EDX confirm the phase purity of $Na_4MnV(PO_4)_3$ and ensure the uniform distribution of reduced graphene oxide over its particles.

2.2. Electrochemical activity in non-aqueous electrolytes

Cyclic voltammetry (CV) was used to determine the voltage positions of the redox couples $V^{4+/3+}$ and $Mn^{3+/2+}$ in the composite $Na_4MnV(PO_4)_3$-rGO. **Figure 3a** shows the first five CV cycles recorded for $Na_4MnV(PO_4)_3$-rGO under the 0.1 mV S^{-1} rate. The first set of redox peaks appears at 3.4 V (anodic) and 3.3 V (cathodic) and corresponds to the electrochemical activity of the $V^{4+/3+}$ redox couple. These two peaks are attributed to the extraction and insertion of Na^+-ions from/into the Na (2) site of the NASICON structure.

A close examination led us to note that the main cathodic peak (3.3V) has an asymmetry due to a second peak (3.35 V) that merged with it to form what appears to be like a single peak (**figure 3**a). The second set of redox peaks is observed at 3.6 V (anodic) and 3.5 V (cathodic) and corresponds to the electrochemical activity of the $Mn^{3+/2+}$ redox couple. These anodic and cathodic peaks are associated with the extraction and insertion of Na^+-ions from/into both the Na (1) and Na (2) sites of $Na_4MnV(PO_4)_3$. Chen et al. found that the oxidation of V^{3+} to V^{4+} is responsible for the extraction of half of the Na^+-ions from the Na (2) site by operando x-ray diffraction. In the same manner, the second set of peaks split into two peaks due to the extraction of 65 % and 35 % Na^+-ions from the Na (1) and Na (2) sites, respectively.[25-26] These interpretations are supported by an earlier crystallographic study.[25-26] The occupancy of sodium ions in Na (1) and Na (2) sites are 1 and 3, respectively.[27]

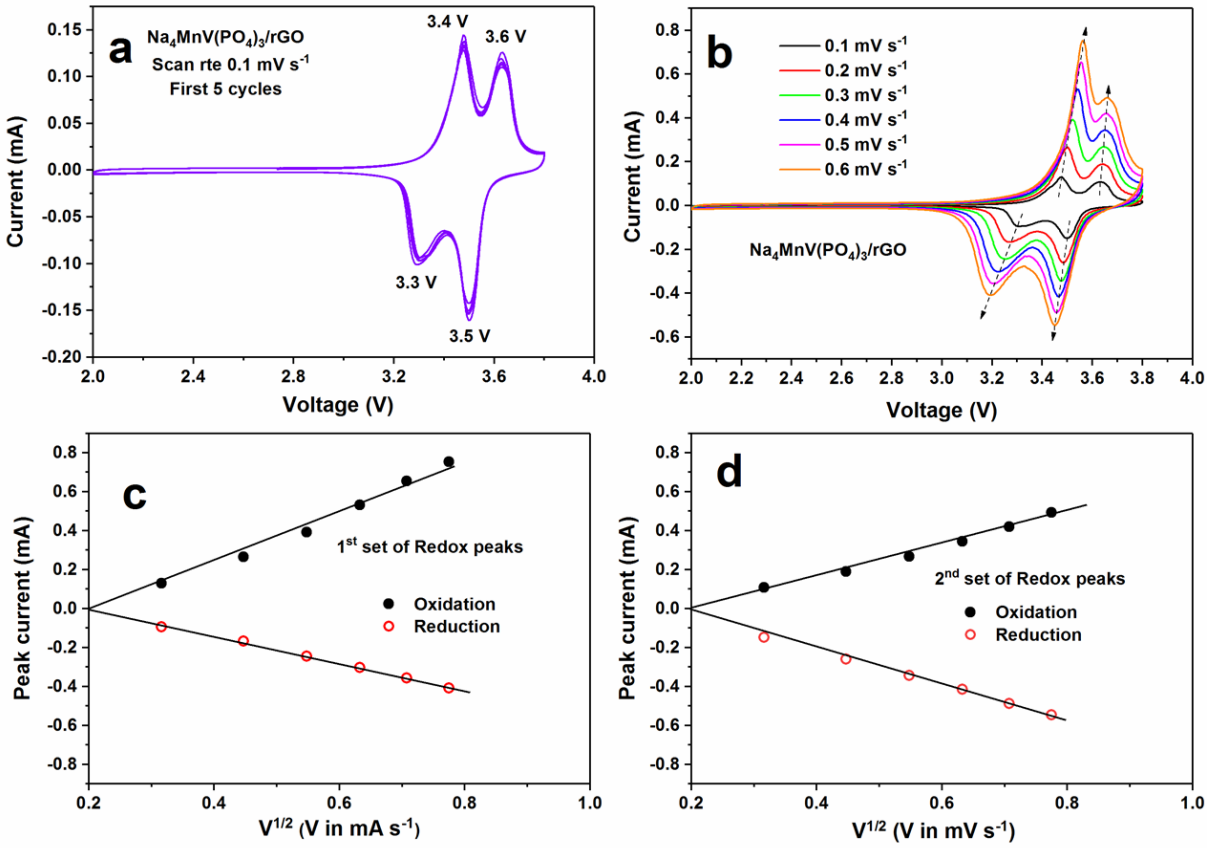

Figure 3: Cyclic voltammetry plots for the $Na_4MnV(PO_4)_3$-rGO composite sample at a) single scan rate of 0.1 mV s^{-1}, b) different scanning rates of 0.1, 0.2, 0.3, 0.4, 0.5 and 0.6 mV s^{-1}. The plots between the peak current and the square root of the scan rate for (c) first set of redox peaks and (d) second set of redox peaks.

Figure 3b shows the CV plots taken under increasing scan rates, 0.1 to 0.6 mV s^{-1}, between 2.0 and 3.8 V. As the scan rate increases, the height and the area of the CV curve increases. The ratio of the anodic-to-cathodic peaks is close to unity, i.e. $|i_{pc}/i_{pa}| = 1$. Of significance, there are no side reactions and only a single-phase mechanism is active during the sodium removal/uptake processes. The linear relationship between the redox peak current and the square root of the scan rate is shown in **figure 3**c and **3d**. The quasi linearity of the plots indicate that the electrochemical process is mostly controlled by diffusion in this intercalation compound.[28]

The galvanostatic charge-discharge cycles were obtained on cells comprising the $Na_4MnV(PO_4)_3$-rGO composite electrodes and cycled between 2.5-3.8 V. Fi**gure 4**a shows

the cycling performance of $Na_4MnV(PO_4)_3$-rGO in a half-cell configuration in the presence of a non-aqueous electrolyte. The cell delivered an initial discharge capacity of 94 mAh g^{-1}, and after 60 cycles the discharge capacity was 86 mAh g^{-1} with 98% coulombic efficiency under C/10 (11 mA g^{-1}). **Figure 4**b displays selected voltage profiles of $Na_4MnV(PO_4)_3$-rGO during charge and discharge at the 0.1 C rate. Each curve shows two plateaus corresponding to $V^{4+/3+}$ and $Mn^{3+/2+}$ redox couples.

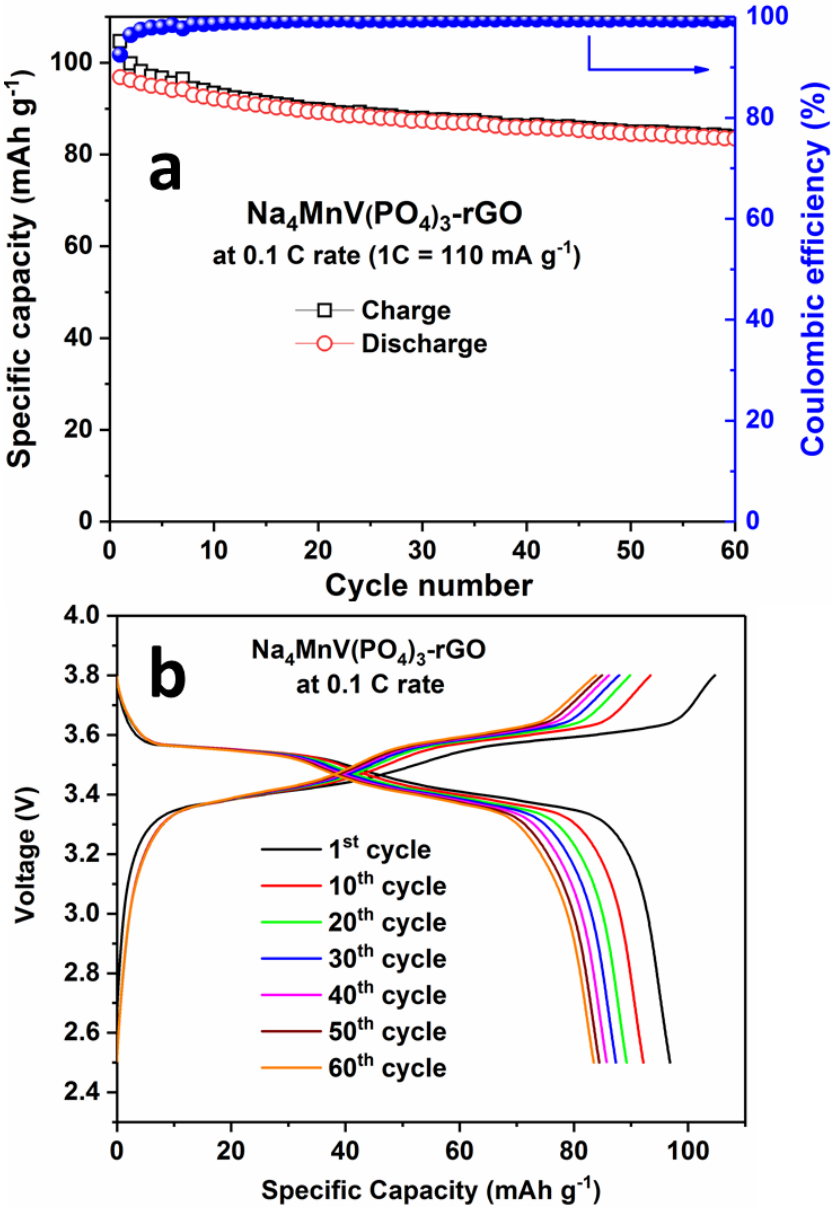

Figure 4: Cycling performance and (b) the corresponding charge-discharge voltage profiles of the $Na_4MnV(PO_4)_3$-rGO composite measured at 0.1 C (11 mA g^{-1}) in non-aqueous electrolytes

Figure 5a shows the rate-capacity trend obtained under increasing current rates, 110 mA g^{-1} (1 C), 220 mA g^{-1} (2 C), 550 mA g^{-1} (5 C), 1.1 A g^{-1} (10 C), and 2.2 A g^{-1} (20 C), and then back to the 1C rate. At the very high current rate (20 C), $Na_4MnV(PO_4)_3$-rGO delivered a stable capacity of 65 mAh g^{-1}. This high rate capability can be attributed to electronically conducting percolating network created by the proper presence of rGO. **Figure 5**b displays the corresponding voltage profiles of $Na_4MnV(PO_4)_3$-rGO obtained under the same rate conditions of **figure 5a**.

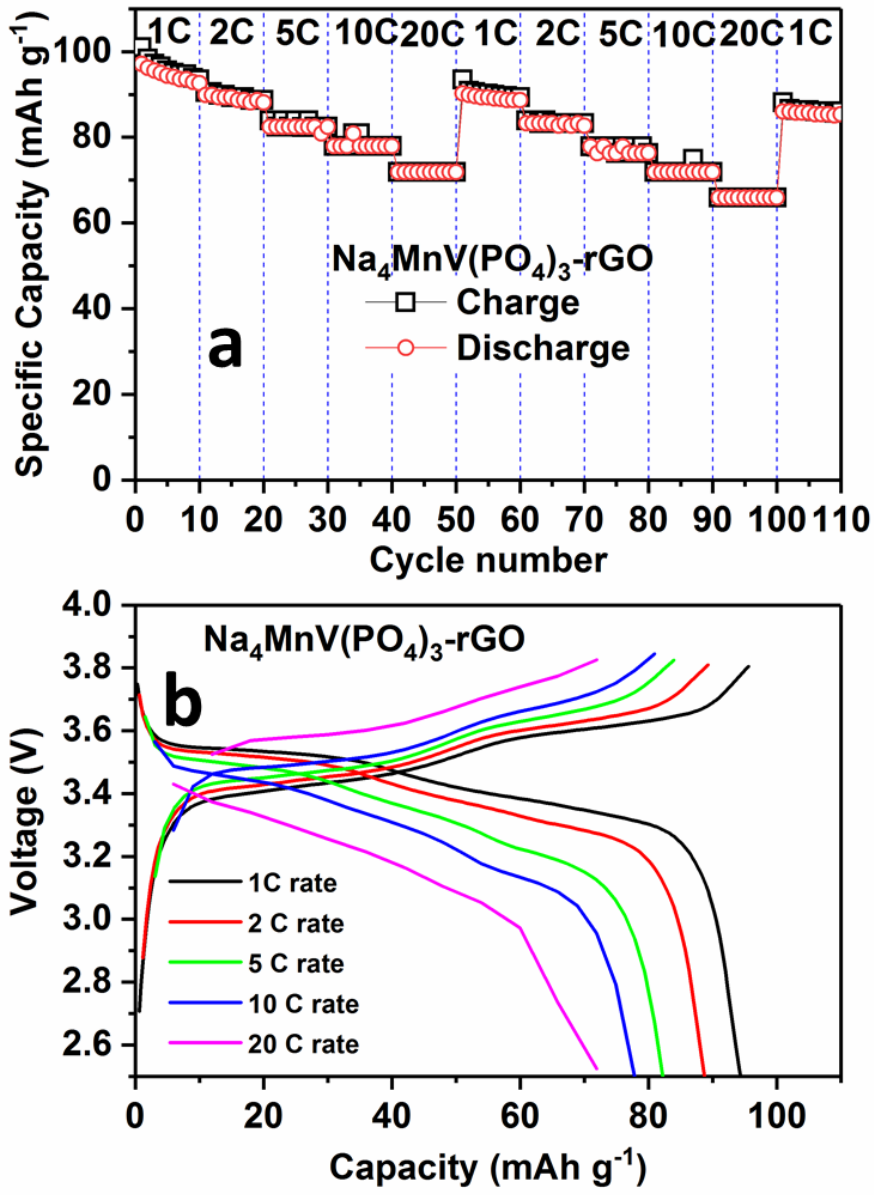

Figure 5: a) Rate performance and (b) representative charge-discharge voltage profiles of the $Na_4MnV(PO_4)_3$-rGO composite measured at different C-rates up to 20 C in non-aqueous electrolytes.

Electrochemical Impedance Spectroscopy (EIS) measurements were recorded during the second cycle at different voltage levels in half cell configurations (**figure S3)**. Here, the symbols represent the experimental data, and the fitted data are represented as continuous black lines. The plots were analyzed by fitting the data with an electrical equivalent circuit using the software *Z-view* (**Figure S3**c), where, R_1 represents the electrolyte resistance; R_2 represents the charge transfer resistance at the sodium/electrolyte interface along with a minor contribution of the electronic resistance of the active particles; R_3 represents the charge transfer resistance at the composite cathode/electrolyte interface; CPE represents the constant phase element, and Ws represents the Warburg impedance. Detailed description of circuit elements, their individual contribution and separation processes can be found in our previous report.[29] **Figure 6** shows the trend of R_1, R_2 and R_3 resistances as a function of cell voltage during the charge-discharge of $Na_4MnV(PO_4)_3$-rGO. R_1 values are constant regardless of states of charge and discharge, which is an indication of a stable ionic resistance of the used electrolyte. During charge, the R_2 values slightly increased till 3.3 V, and then gradually decreased with further charging up to the higher cutoff voltage (3.8 V). During discharge, the reverse trend was observed, i.e. R_2 values increased till 3.5 V and remained quite constant on further discharging down to the lower cutoff voltage (2.6 V). Such a behavior is not clearly understood. However, the electronic conductivity of the active particle changes with states of charge/discharge, and therefore, R_2 can be impacted since the electronic resistance of the active material is included with the charge transfer resistance at the sodium/electrolyte interface due to similar capacitance values and relaxation times. It is clear from **Figure 6** that R_3 initially increased during charge (up to 3 V), then gradually decreased on further charging up to the higher cutoff voltage 3.8 V, and the opposite trend was observed during discharge (**Figure 6**).

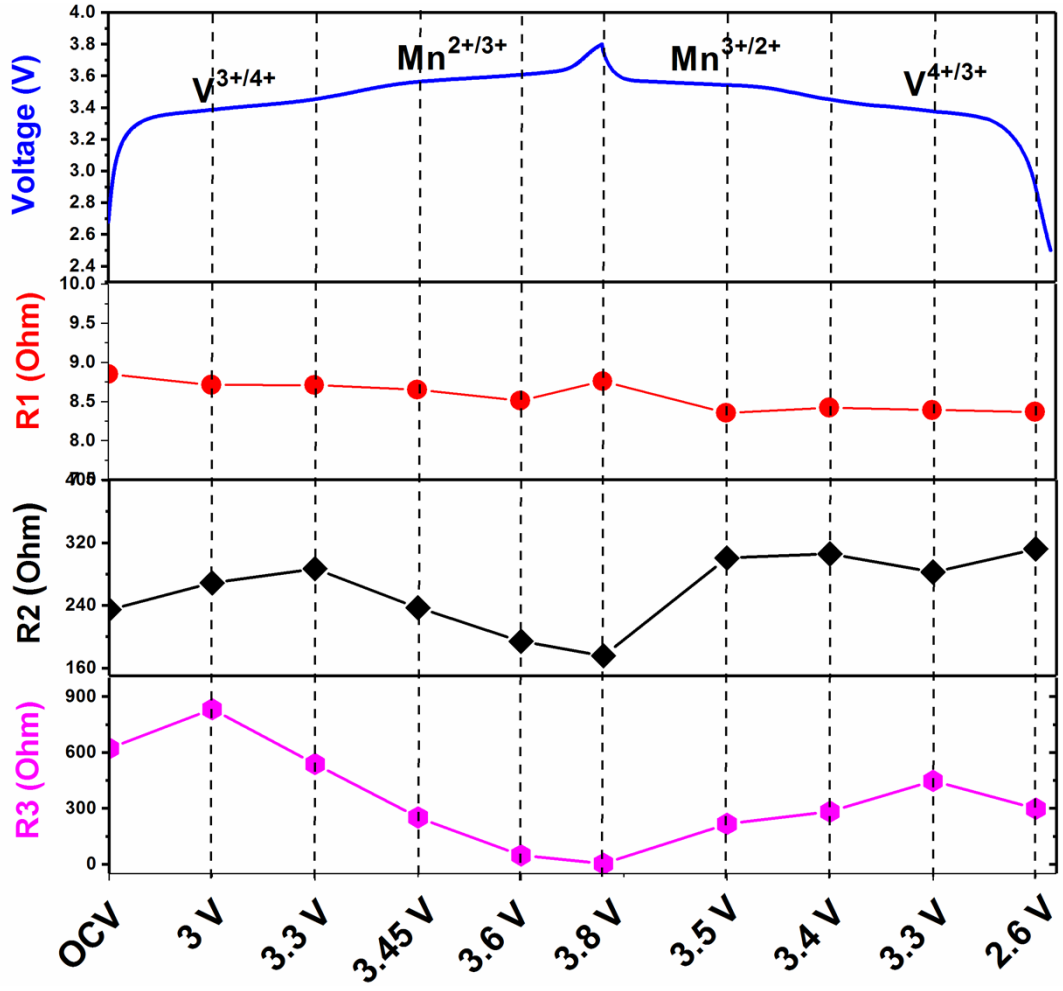

Figure 6: Changes in R1, R2 & R3 resistances with respect to different voltages during the charge/discharge cycle.

It should be noted that both vanadium and manganese form mixed valence states during charge and discharge, and this can have a significant impact on the electronic conductivity of the active particle, and particularly on R3. It appears that the oxidation of vanadium (from 3^+ to 4^+) has less impact on the electronic conductivity of the active particle during the first half of charge. On the contrary, the formation of manganese mixed valence (Mn^{2+} and Mn^{3+}) on further charge has a pronounced impact on the electronic conductivity of the active material, and therefore promotes the charge transfer kinetics at the composite cathode/electrolyte interface. Indeed, during the second half of charge, the concentration of Mn^{3+} gradually increases and the electronic conductivity increases as the R_3 resistance decreases; whereas, the

opposite phenomenon occurs during discharge (**figure 6)**. The results imply that the intrinsic electronic conductivity plays an important role in the charge transfer mechanism at the cathode/electrolyte interface.

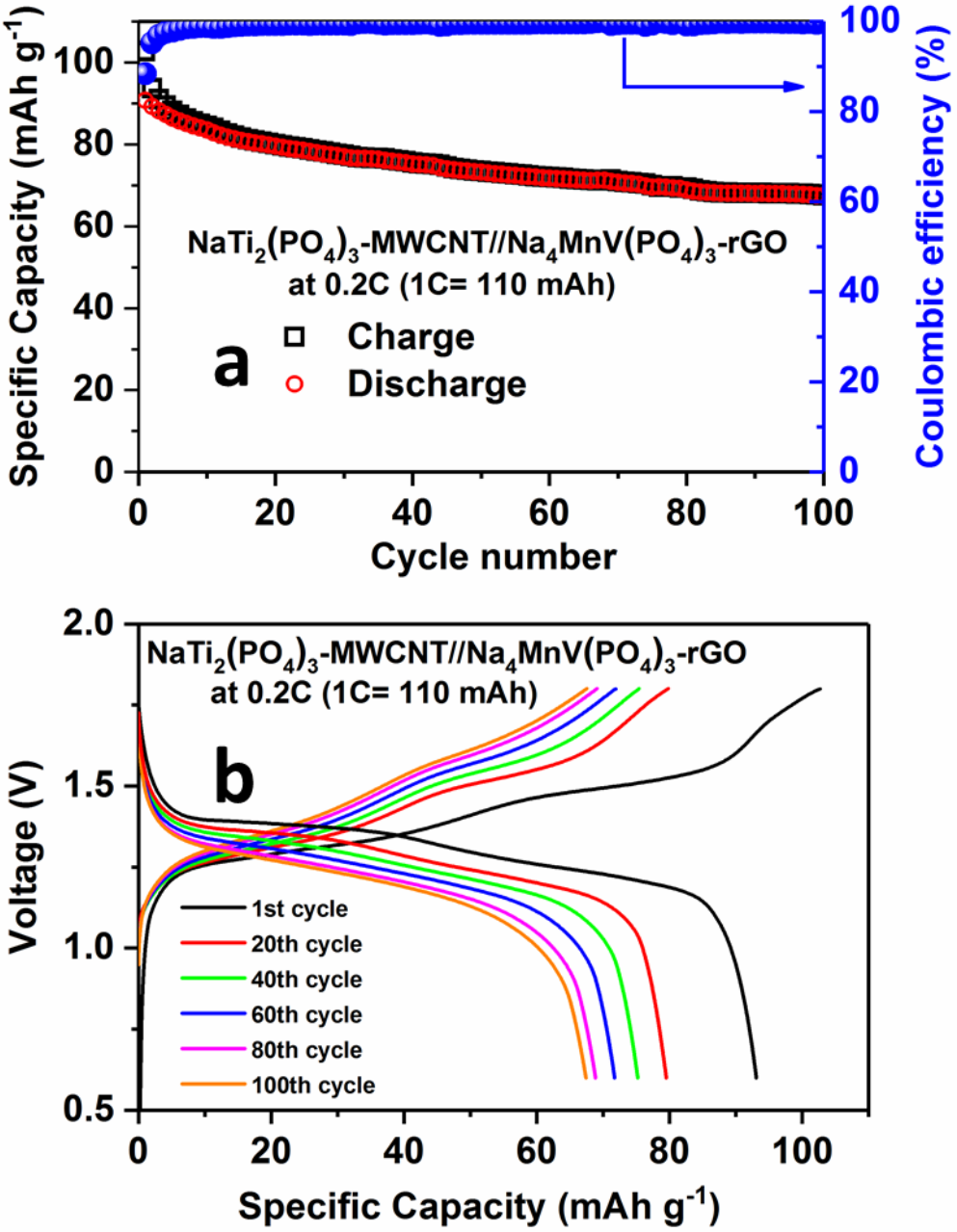

Figure 7: (a) Cycling performance and coulombic efficiencies at 0.2 C rate, (b) charge - discharge curves of the $NaTi_2(PO_4)_3$-MWCNT//$Na_4MnV(PO_4)_3$-rGO full-cell in non-aqueous electrolytes.

Figure 7 displays the performance of the cell comprising $NaTi_2(PO_4)_3$-MWCNT//$Na_4MnV(PO_4)_3$-rGO and a non-aqueous electrolyte, and cycled between 0.6-1.8 V at the 0.2 C rate. The full-cell delivers an initial discharge capacity of 92 mAh g^{-1} at a rate of 0.2 C (22 mA g^{-1}) with 90 % coulombic efficiency (**figure 7**a). The discharge capacity decreased to 68 mAh g^{-1} after 100 cycles; however, the efficiency gradually increased to 99 % after being 90 % initially. **Figure 7**b shows selected charge-discharge voltage profiles for different cycles numbers. The cell $NaTi_2(PO_4)_3$-MWCNT//$Na_4MnV(PO_4)_3$-rGO shows an average discharge voltage around 1.3 V.

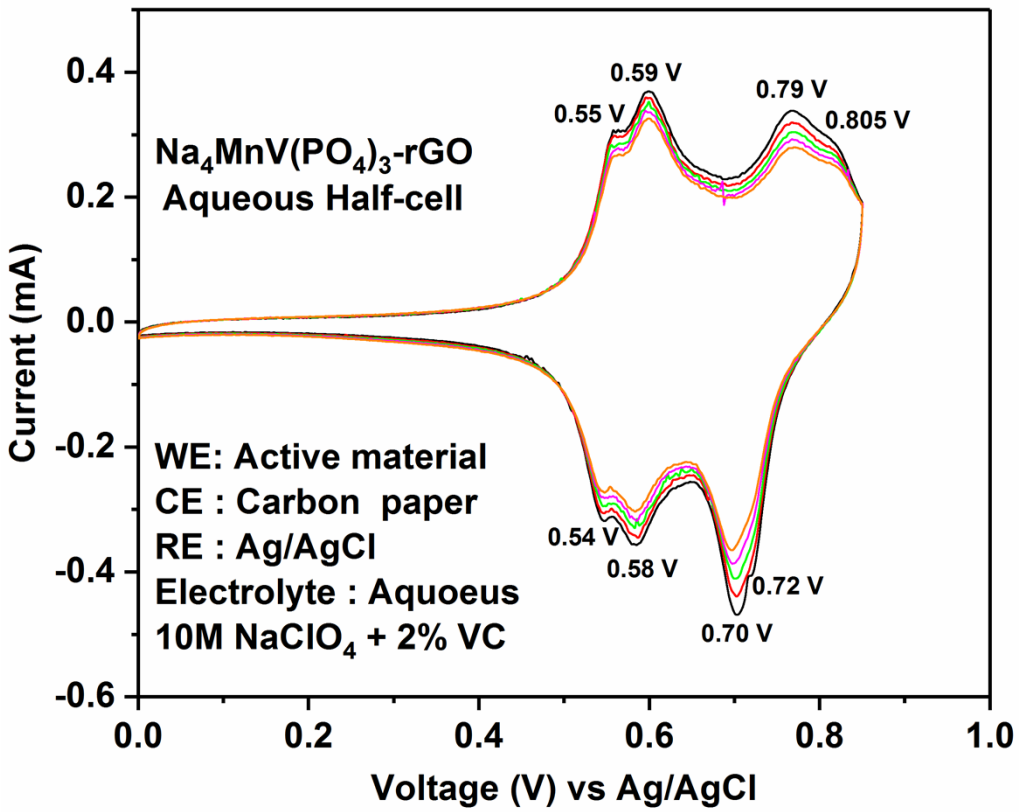

Figure 8: Cyclic voltammetry plots for the $Na_4MnV(PO_4)_3$-rGO composites at 0.2 mV S^{-1} in aqueous electrolytes

3.3. Electrochemical activity in aqueous electrolytes

The electrochemical performance of the cathode $Na_4MnV(PO_4)_3$-rGO was checked with different aqueous electrolytes solutions, (1 M Na_2SO_4, 5 M $NaClO_4$ and 10 M $NaClO_4$ with 2 v.% vinylene carbonate (VC)), in half cell configurations. **Figure S4** shows the charge-

discharge curves of $Na_4MnV(PO_4)_3$-rGO in aqueous half-cells containing two electrolytes (1 M Na_2SO_4 and 5 M $NaClO_4$). 10 M $NaClO_4$ (with 2 % VC) provides better cycle life and good capacity retention compared to the other electrolyte formulations. It should be noted that an optimum high electrolyte concentration (e.g. 10 M) exhibits higher ionic conductivity. In view of these results, the best electrolyte formulation, 10 M $NaClO_4$ (with 2 % VC), was selected for further studies.[30] **Figure 8** shows the cyclic voltammetry plots measured between 0 and 0.8 V vs. Ag/AgCl for a cell containing $Na_4MnV(PO_4)_3$-rGO electrode and the electrolyte solution 10 M $NaClO_4$ (with 2 % VC). It should be noted that two voltage plateaus were obtained in normal charge-discharge process. However, splitting of peaks corresponding to $V^{4+/3+}$ and $Mn^{3+/2+}$ redox couples were observed in the CV measurements (cf. **figure 8)**. In order to corroborate the above peak splitting in CV plots, we again measured the charge-discharge profile of $Na_4MnV(PO_4)_3$-rGO under slow current rate, i.e. 0.05 C, in non-aqueous electrolyte (**Figure S5)**. In that case, two main sloppy voltage plateaus were observed (**Figure S5**a) likely observed in **Figure 4**b for fast charge-discharge process. However, differentiation (dQ/dV) of capacity vs. voltage plot reveals two sub-voltage regimes in each of these voltage plateaus (F**igure S5**b). The behavior of the peak splitting is not clearly understood as only two different sodium sites [Na(1) and Na(2)] are available in the crystal structure. It is known that removal of sodium switching from Na(2) site to Na(1) site depending on the energetic favorability (state of charge and discharge). We speculate that each plateau may have additional energetic sites those are responsible for the spitting of the peak. Details understanding of such behavior is under progress by experimental and simulation studies.

Figure 9 shows the cyclic stability for the $Na_4MnV(PO_4)_3$-rGO composite at 1C (110 mAh g^{-1}) and 10 C for 50 cycles in a voltage range of 0-0.82 V vs. Ag/AgCl. The half-cell delivers an initial discharge capacity of 92 mAh g^{-1}, and 82 % of the initial capacity was retained after 10 cycles at 1 C rate. At higher rate (10 C), $Na_4MnV(PO_4)_3$-rGO composite delivers a stable capacity of 60 mAh g^{-1} for 40 cycles. The charge-discharge voltage profiles for each cycle is

shown in **figure 9**b. The average voltage of $Na_4MnV(PO_4)_3$-rGO electrode in aqueous electrolytes is 0.66 vs. Ag/AgCl. The SEM image and cyclic voltammetry results of the $NaTi_2(PO_4)_3$-MWCNT sample in 10 M $NaClO_4$ (with 2 % VC) are shown in **figure S9**.[31]

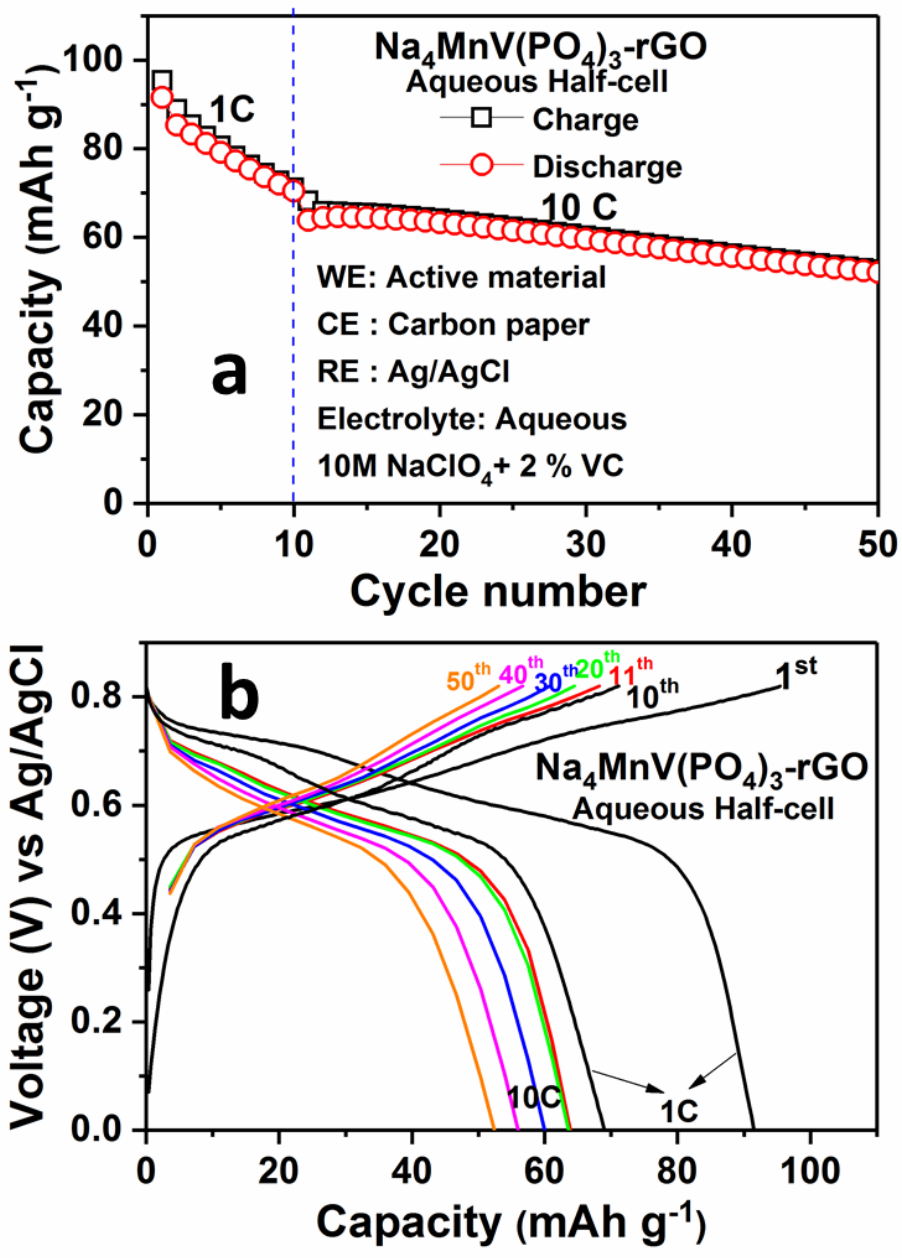

Figure 9: a) Cycling performance b) charge-discharge curves at 1 C and 10 C rates for the $Na_4MnV(PO_4)_3$-rGO composite in aqueous electrolytes.

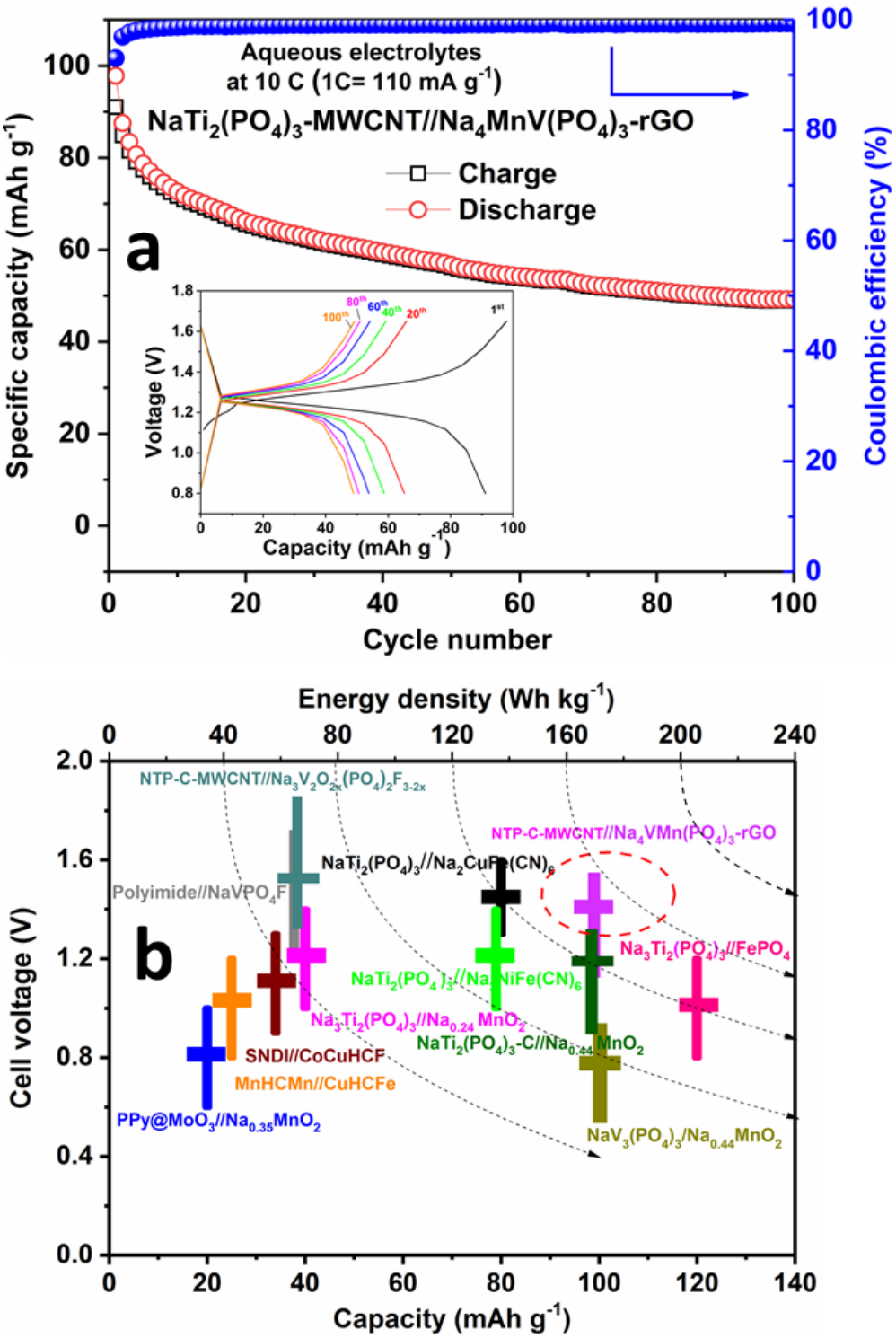

Figure 10: a) Cycling performance and coulombic efficiencies at 10 C rate (insert figure charge discharge curves) for the $NaTi_2(PO_4)_3$-MWCNT//$Na_4MnV(PO_4)_3$-rGO full-cell in aqueous electrolytes. b) Comparison of the capacity, energy density and full-cell voltages reported for aqueous sodium-ion batteries.

Figure 10 shows the electrochemical performances of an aqueous full-cell fabricated with $NaTi_2(PO_4)_3$-MWCNT//$Na_4MnV(PO_4)_3$-rGO. **Figure 10**a shows the cycling performance of the aqueous full-cell in the voltage range 0.8 V-1.65 V at 10 C rate (1.1 A g^{-1}). The initial discharge capacity of the aqueous cell was 97 mAh g^{-1}, and after 60 cycles, it stabilized at 50 mAh g^{-1} with 99% coulombic efficiency. **Figure 10**a shows the charge-discharge voltage profiles for each cycle. **Figure 10b** provides a comparison between the aqueous sodium-ion battery systems that were reported so far: $NaTi_2(PO_4)_3$ // $Na_{0.44}MnO_2$,[21] $Na_3Ti_2(PO_4)_3$ // $Na_{0.24}MnO_2$,[31] $NaTi_2(PO_4)_3$ // $Na_2CuFe(CN)_6$,[32] $NaTi_2(PO_4)_3$ // $Na_2NiFe(CN)_6$,[33] disodium naphthalene diimide (SNDI) // cobalt & copper hexacyanoferrate (CoCuHCF),[34] manganese hexacyanomanganate (MnHCMn) // copper hexacyanoferrate (CuHCFe),[15c] PPy@MoO_3 // $Na_{0.35}MnO_2$,[35] polyimide // $NaVPO_4F$,[36] $Na_3Ti_2(PO_4)_3$ // $Na_3V_2O_{2x}(PO_4)_2F_{3-2x}$-MWCNT,[23] and $NaV_3(PO_4)_3$ // $Na_{0.44}MnO_2$.[37] The full-cell characteristics from our study are on the higher ends in terms of voltage and capacity compared to the other systems. The average voltage for the cell $NaTi_2(PO_4)_3$-MWCNT // $Na_4MnV(PO_4)_3$-rGO is 1.38 V. The most promising outcome is that the cell delivers an energy density exceeding 140 Wh kg^{-1}, which is the highest energy density of an aqueous sodium-ion battery with intercalation anode and cathode, so far. However, the capacity fade on cycling remains the issue to be solved.

3. Conclusion

The $Na_4MnV(PO_4)_3$ was synthesized with reduced graphene oxide (rGO) by the simple sol-gel method. The composite was characterized by XRD, SEM, TGA and TEM-EDX techniques to confirm the phase purity and microstructural properties. The synthesized $Na_4MnV(PO_4)_3$-rGO composite was tested as a cathode material in both aqueous and non-aqueous electrolytes using half-cell and full-cell configurations. The half-cell delivers a stable discharge capacity of 86 mAh g^{-1} after 100 cycles at C/10 rate, and can tolerate a very high current rate of 20 C in a non-aqueous electrolyte. The enhanced performance is mainly due to

the fast mass transport in the NASICON structure and the improved electronic conductivity in rGO network that is homogenously integrated with the active particles. The assembled full cell with $NaTi_2(PO_4)_3$-MWCNT exhibits a discharge capacity of 68 mAh g^{-1} after 100 cycles at the 0.2 C rate. $Na_4MnV(PO_4)_3$ shows the initial discharge capacity of 92 mAh g^{-1} at 1 C rate in aqueous electrolyte in a half-cell, and 97 mAh g^{-1} at 10 C rate when coupled with $NaTi_2(PO_4)_3$-MWCNT. So far, the energy density (140 Wh kg^{-1}) of the battery aqueous system $NaTi_2(PO_4)_3$-MWCNT//$Na_4MnV(PO_4)_3$-rGO is superior to the reported aqueous sodium-ion battery systems containing intercalation cathodes and anodes. Aware of the need for further performance enhancement, the present results, however, shed the light on the potential that $Na_4MnV(PO_4)_3$-rGO could have in enabling the implementation of aqueous and non-aqueous sodium-ion batteries in stationary battery applications.

4. Experimental Section

Synthesis of $Na_4MnV(PO_4)_3$-rGO composite

$Na_4MnV(PO_4)_3$-rGO composite was prepared by sol-gel method. In this case, we have used Na-acetate, Mn-acetate, $NH_4H_2PO_4$, V_2O_5 (all Sigma-Aldrich), and graphene oxide (GO) as precursors. First V_2O_5 and citric acid (2 gm) were dissolved in 20 ml of H_2O and stirred at 80 ^oC to form a clear blue solution (Solution A). Then, Na-acetate and GO were also added into solution A. $NH_4H_2PO_4$ and Mn-acetate were dissolved in 10 ml of H_2O (Solution B). After stirring at 80 ^oC for 30 min, solution B was added slowly to the solution A and the final solution was continuously stirred at 80 ^oC for 12 hr. Thereafter, the gel was transferred into an oven and heated up to 180 ^oC for 3 hr. Then, the dry gel was ground and calcinated under argon atmosphere at 750 ^oC for 9 hr. to obtained pure $Na_4MnV(PO_4)_3$-rGO composite. A detailed procedure can be found in reference.[13]

Characterization

The purity of $Na_4MnV(PO_4)_3$-rGO composite was checked by x-ray diffraction (Bruker, Advance D8) with a Cu-Kα radiation (λ=1.5418 Å) at room temperature. The particle size and

morphology were characterized using the field-emission scanning electron microscope (FE-SEM, FEI, Quanta 650). A transmission electron microscope (TEM, Talos F200X, FEI) with a 200 kV operating voltage was used to capture the morphology, EDX spectrum and SAED patterns of the $Na_4VMn(PO_4)_3$-rGO composite. Carbon content was determined by TG analysis using a TA instrument (TGA800) under synthetic air atmosphere.

The electrochemical studies were carried out using $Na_4MnV(PO_4)_3$-rGO assembled with a non-aqueous electrolyte in CR2032 coin cells. The electrode composition was 80 wt.% active material, 10 wt.% Super-P carbon and 10 wt.% polyvinylidene fluoride (PVDF) binder in the N-Methyl-2-pyrrolidone (NMP) solvent. The slurry was coated onto an Al-foil. The latter was cut into disc electrodes with a diameter of 14.5 mm. Sodium metal was used as the anode, and 1 M $NaClO_4$ in Propylene Carbonate (PC) with 5 vol.% of Fluoro-Ethylene Carbonate (FEC) was used as the electrolytes. The coin cells were assembled in an argon-filled glove box using a borosilicate glass-fiber separator (Whatman GF/D). In the full-cell tests, the composite $NaTi_2(PO_4)_3$-MWCNT was coated onto an Al-foil and used as the anode. The loading densities of $Na_4VMn(PO_4)_3$-rGO and $NaTi_2(PO_4)_3$-MWCNT were 0.8 and 1.5 g/cm^2, respectively. The cyclic voltammetry and galvanostatic cycling of the cells were carried out using the potentiostat VMP3 (Biologic) and battery cycler (Arbin). The half cells were cycled between 2.5 and 3.8 V, and the full cells were cycled between 0.6 and 1.8 V.

In the case of the aqueous electrolyte, the $Na_4VMn(PO_4)_3$-rGO based slurry was coated onto a carbon paper and cut into 10 mm squares and 14.5 mm diameter disc electrodes. In the half-cell configuration, the active material-coated carbon paper and a bare carbon paper (3 times bigger) were used as the working and counter electrodes, respectively. Ag/AgCl electrode was used as the reference electrode. 1 M Na_2SO_4, 5 M $NaClO_4$, and 10 M $NaClO_4$ with 2 v.% Vinylene Carbonate (VC) dissolved in double distilled water were used as electrolytes. In the full-cell configuration, $NaTi_2(PO_4)_3$-MWCNT coated onto a carbon paper was used as the anode. Beaker-type half-cells were cycled between 0 and 0.82 V in a galvanostatic mode

using the potentiostat VMP3 (Biologic, SP-300) at 1 C and 10 C rates. The $NaTi_2(PO_4)_3$-MWCNT/$Na_4MnV(PO_4)_3$-rGO cells were cycled between 0.8 and 1.65 V at the 10 C rate based on the cathode material weight.

Supporting Information
Supporting Information is available from the Wiley Online Library or from the author.

Acknowledgements

Authors thank to Core Lab, Qatar Environment and Energy Research Institute (QEERI) for providing characterization facilities. The authors would like to thank Dr. H. B. Yahia, QEERI for much helpful discussion. Authors gratefully acknowledge financial support from National Priorities Research Program (NPRP9-263-2-122) funded by Qatar National Research Fund (QNRF).

Received: ((will be filled in by the editorial staff))
Revised: ((will be filled in by the editorial staff))
Published online: ((will be filled in by the editorial staff))

References

[1] a) J. B. Goodenough, K.-S. Park, *Journal of the American Chemical Society* **2013**, 135, 1167; b) M. Sawicki, L. L. Shaw, *RSC Advances* **2015**, 5, 53129.
[2] N. Yabuuchi, I. Ikeuchi, K. Kubota, S. Komaba, *ACS applied materials & interfaces* **2016**, 8, 32292.
[3] R. Ruffo, R. Fathi, D. J. Kim, Y. H. Jung, C. M. Mari, D. K. Kim, *Electrochimica Acta* **2013**, 108, 575.
[4] J. Y. Hwa, C. A. S., J. R. E., N. Poul, K. D. Kyung, *Advanced Functional Materials* **2015**, 25, 3227.
[5] C. Li, X. Miao, W. Chu, P. Wu, D. G. Tong, *Journal of Materials Chemistry A* **2015**, 3, 8265.
[6] H. Ben Yahia, R. Essehli, R. Amin, K. Boulahya, T. Okumura, I. Belharouak, *Journal of Power Sources* **2018**, 382, 144.
[7] R. Essehli, H. Ben Yahia, K. Maher, M. T. Sougrati, A. Abouimrane, J. B. Park, Y. K. Sun, M. A. Al-Maadeed, I. Belharouak, *Journal of Power Sources* **2016**, 324, 657.
[8] P. R. Kumar, Y. H. Jung, J. E. Wang, D. K. Kim, *Journal of Power Sources* **2016**, 324, 421.
[9] a) K. Hyungsub, K. Haegyeom, D. Zhang, L. M. Hwan, L. Kyungmi, Y. Gabin, K. Kisuk, *Advanced Energy Materials* **2016**, 6, 1600943; b) Y. Liu, X. Liu, T. Wang, L.-Z. Fan, L. Jiao, *Sustainable Energy & Fuels* **2017**, 1, 986; c) K. Sung‐Wook, S.

Dong‐Hwa, M. Xiaohua, C. Gerbrand, K. Kisuk, *Advanced Energy Materials* **2012**, 2, 710.
[10] Y. Jiang, X. Zhou, D. Li, X. Cheng, F. Liu, Y. Yu, *Advanced Energy Materials* **2018**, 8, 1800068.
[11] W. Zhou, L. Xue, X. Lü, H. Gao, Y. Li, S. Xin, G. Fu, Z. Cui, Y. Zhu, J. B. Goodenough, *Nano letters* **2016**, 16, 7836.
[12] A. Yamada, M. Hosoya, S.-C. Chung, Y. Kudo, K. Hinokuma, K.-Y. Liu, Y. Nishi, *Journal of Power Sources* **2003**, 119-121, 232.
[13] H. Li, T. Jin, X. Chen, Y. Lai, Z. Zhang, W. Bao, L. Jiao, *Advanced Energy Materials* **2018**, 8, 1801418.
[14] J. B. Robinson, D. P. Finegan, T. M. M. Heenan, K. Smith, E. Kendrick, D. J. L. Brett, P. R. Shearing, *Journal of Electrochemical Energy Conversion and Storage* **2017**, 15, 011010.
[15] a) H. Pan, Y.-S. Hu, L. Chen, *Energy & Environmental Science* **2013**, 6, 2338; b) Z. Yang, J. Zhang, M. C. W. Kintner-Meyer, X. Lu, D. Choi, J. P. Lemmon, J. Liu, *Chemical Reviews* **2011**, 111, 3577; c) M. Pasta, C. D. Wessells, N. Liu, J. Nelson, M. T. McDowell, R. A. Huggins, M. F. Toney, Y. Cui, *Nature Communications* **2014**, 5, 3007.
[16] a) H. Kim, J. Hong, K.-Y. Park, H. Kim, S.-W. Kim, K. Kang, *Chemical Reviews* **2014**, 114, 11788; b) X. Dong, L. Chen, J. Liu, S. Haller, Y. Wang, Y. Xia, *Science Advances* **2016**, 2.
[17] J. Köhler, H. Makihara, H. Uegaito, H. Inoue, M. Toki, *Electrochimica Acta* **2000**, 46, 59.
[18] H. Wang, K. Huang, Y. Zeng, S. Yang, L. Chen, *Electrochimica Acta* **2007**, 52, 3280.
[19] D. Sun, Y. Tang, K. He, Y. Ren, S. Liu, H. Wang, *Scientific reports* **2015**, 5, 17452.
[20] S. I. Park, I. Gocheva, S. Okada, J.-i. Yamaki, *Journal of The Electrochemical Society* **2011**, 158, A1067.
[21] Z. Li, D. Young, K. Xiang, W. C. Carter, Y.-M. Chiang, *Advanced Energy Materials* **2012**, 3, 290.
[22] B. Zhang, Y. Liu, X. Wu, Y. Yang, Z. Chang, Z. Wen, Y. Wu, *Chemical communications* **2014**, 50, 1209.
[23] P. R. Kumar, Y. H. Jung, C. H. Lim, D. K. Kim, *Journal of Materials Chemistry A* **2015**, 3, 6271.
[24] a) J. Liu, C. Xu, Z. Chen, S. Ni, Z. X. Shen, *Green Energy & Environment* **2018**, 3, 20; b) D. Reber, R.-S. Kühnel, C. Battaglia, *Meeting Abstracts* **2018**, MA2018-01, 404; c) A. Orita, M. G. Verde, M. Sakai, Y. S. Meng, *Journal of Power Sources* **2016**, 321, 126; d) A. Konarov, D. Gosselink, Y. Zhang, Y. Tian, D. Askhatova, P. Chen, *ECS Electrochemistry Letters* **2015**, 4, A151.
[25] F. Chen, V. M. Kovrugin, R. David, O. Mentré, F. Fauth, J.-N. Chotard, C. Masquelier, *Small Methods* **2018**, 0, 1800218.
[26] U. Nisar, R. A. Shakoor, R. Essehli, R. Amin, B. Orayech, Z. Ahmad, P. R. Kumar, R. Kahraman, S. Al-Qaradawi, A. Soliman, *Electrochimica Acta* **2018**, 292, 98.
[27] Y. Deng, C. Eames, L. H. B. Nguyen, O. Pecher, K. J. Griffith, M. Courty, B. Fleutot, J.-N. Chotard, C. P. Grey, M. S. Islam, C. Masquelier, *Chemistry of Materials* **2018**, 30, 2618.
[28] M. Law, V. Ramar, P. Balaya, *RSC Advances* **2015**, 5, 50155.
[29] R. Amin, I. Belharouak, *Journal of Power Sources* **2017**, 348, 318.
[30] P. R. Kumar, Y. H. Jung, B. Moorthy, D. K. Kim, *Journal of The Electrochemical Society* **2016**, 163, A1484.
[31] Z. Li, D. B. Ravnsbæk, K. Xiang, Y.-M. Chiang, *Electrochemistry Communications* **2014**, 44, 12.

[32] X.-y. Wu, M.-y. Sun, Y.-f. Shen, J.-f. Qian, Y.-l. Cao, X.-p. Ai, H.-x. Yang, *ChemSusChem* **2014**, 7, 407.
[33] X. Wu, Y. Cao, X. Ai, J. Qian, H. Yang, *Electrochemistry Communications* **2013**, 31, 145.
[34] D. J. Kim, Y. H. Jung, K. K. Bharathi, S. H. Je, D. K. Kim, A. Coskun, J. W. Choi, *Advanced Energy Materials* **2014**, 4, 1400133.
[35] Y. Liu, B. H. Zhang, S. Y. Xiao, L. L. Liu, Z. B. Wen, Y. P. Wu, *Electrochimica Acta* **2014**, 116, 512.
[36] H. Qin, Z. P. Song, H. Zhan, Y. H. Zhou, *Journal of Power Sources* **2014**, 249, 367.
[37] L. Ke, J. Dong, B. Lin, T. Yu, H. Wang, S. Zhang, C. Deng, *Nanoscale* **2017**, 9, 4183.

Highlights & TOC figure

The electrochemical performances of $Na_4MnV(PO_4)_3$–rGO in aqueous and non-aqueous electrolytes are explore. Interestingly in aqueous electrolytes, it shows the initial discharge capacity of 92 mAh g^{-1} at 1 C-rate in half-cell and full-cell with $NaTi_2(PO_4)_3$-MWCNT exhibits 97 mAh g^{-1} at 10 C-rate. To the best of our knowledge, the energy density (140 Wh kg^{-1}) of the $NaTi_2(PO_4)_3$-MWCNT//$Na_4MnV(PO_4)_3$-rGO full cell is superior to those reported for any other aqueous sodium ion battery systems.

$Na_4MnV(PO_4)_3$-rGO as Advanced Cathode for Aqueous and Non-Aqueous Sodium Ion Batteries

P. Ramesh Kumar, Aziz Kheireddine, Umair Nisar, R. A. Shakoor, Rachid Essehli, Ruhul Amin and Ilias Belharouak

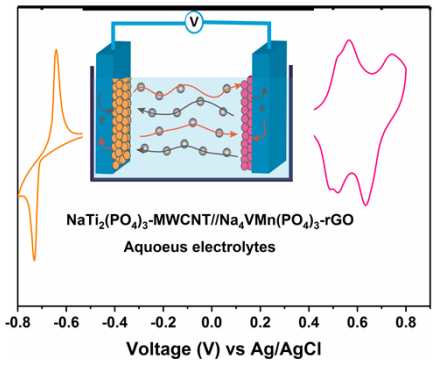

Supporting Information

$Na_4MnV(PO_4)_3$-rGO as Advanced Cathode for Aqueous and Non-Aqueous Sodium Ion Batteries

*P. Ramesh Kumar, Aziz Kheireddine, Umair Nisar, R. A. Shakoor , Rachid Essehli, Ruhul Amin * and Ilias Belharouak **

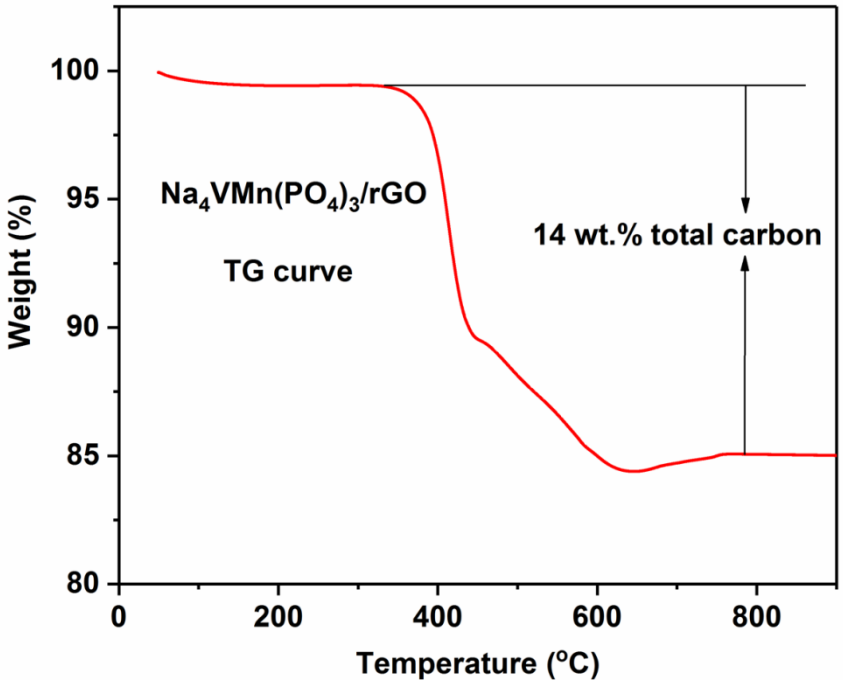

Figure S1: Thermo-gravimetric analysis plot for $Na_4MnV(PO_4)_3$-rGO composite.

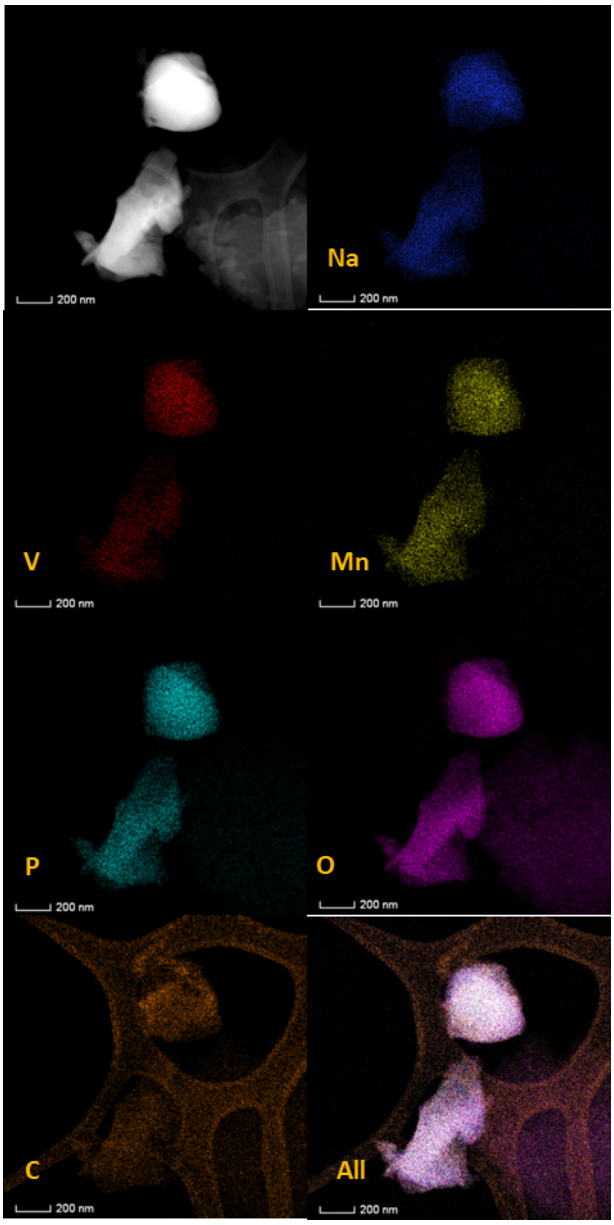

Figure S2: EDX mapping of single $Na_4MnV(PO_4)_3$ particle.

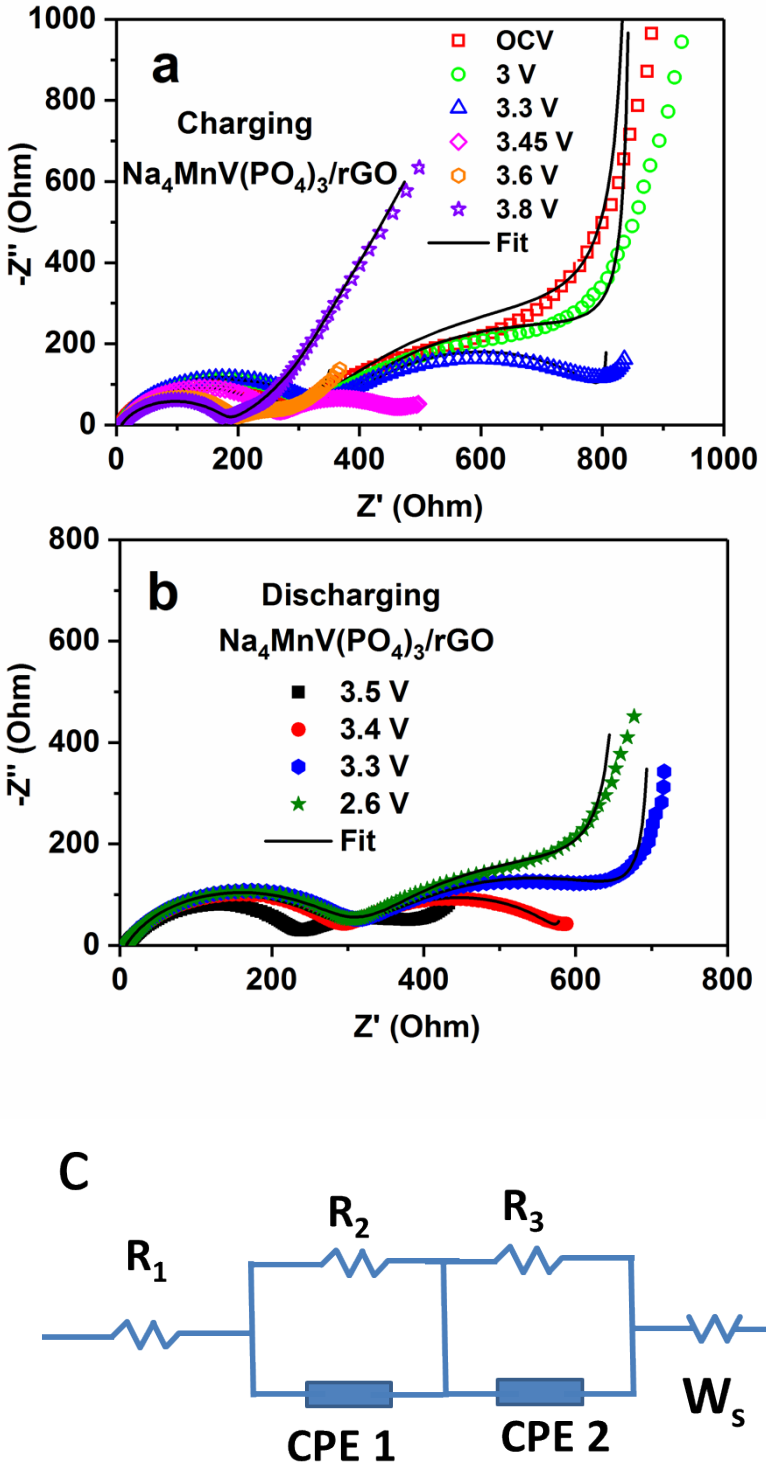

Figure S3: Nyquist plots for $Na_4MnV(PO_4)_3$-rGO at a) charging state and b) discharging states; c) electrical equivalent circuit for fitted data.

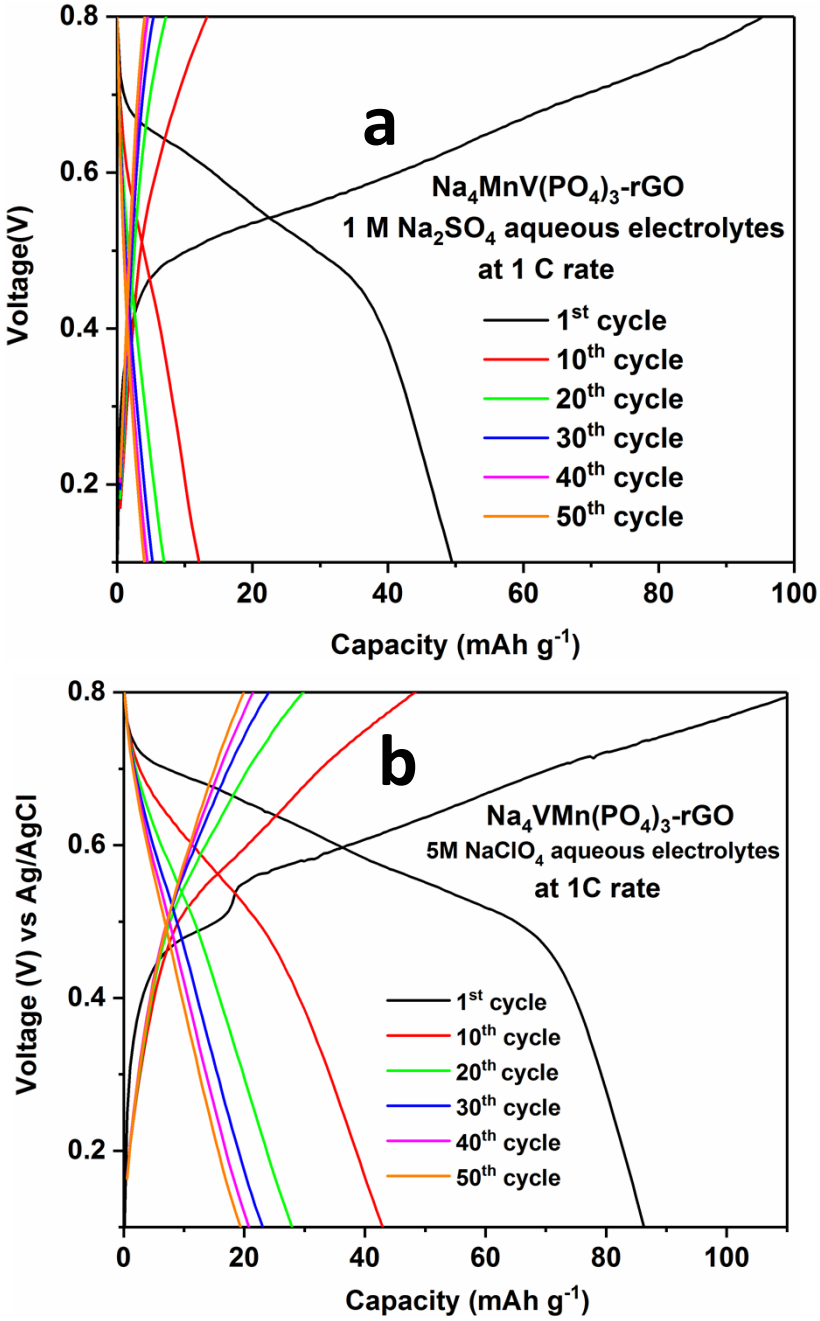

Figure S4: Charge-discharge curves for 50 cycles in a) 1M Na_2SO_4 and b) 5M $NaClO_4$ aqueous electrolytes.

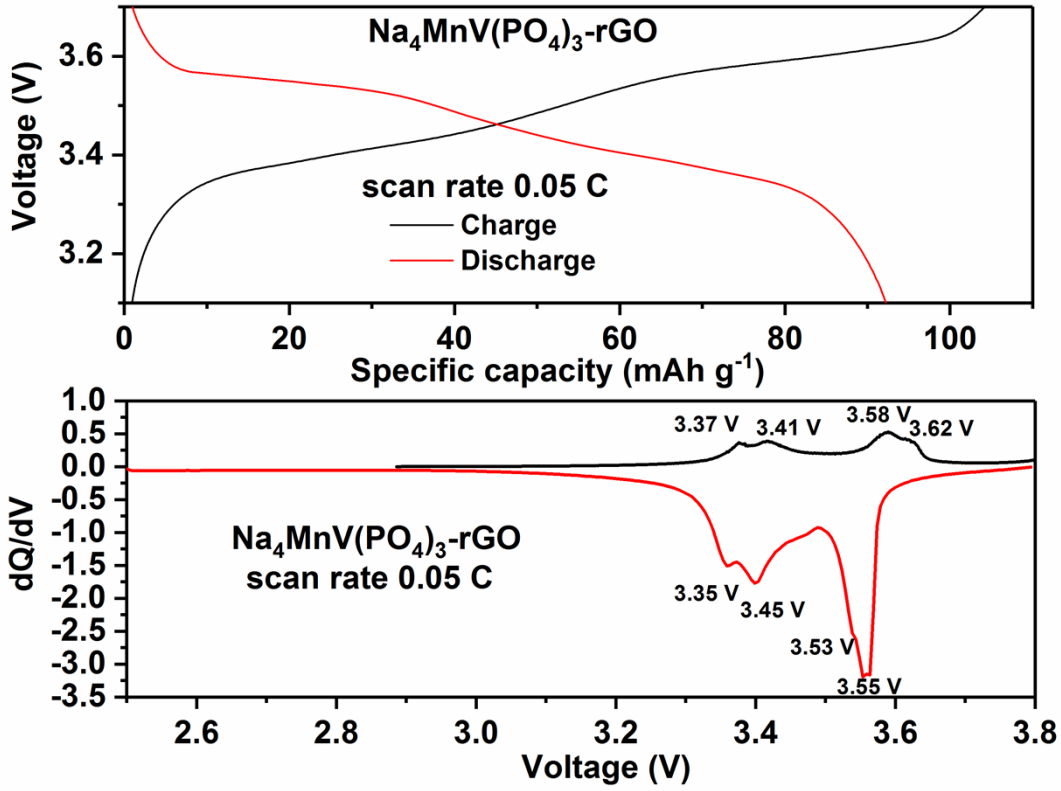

Figure S5: a) Charge-discharge curves at 0.05 C and b) derivative of capacity versus voltage plot for $Na_4MnV(PO_4)_3$-rGO composite in non-aqueous electrolyte.

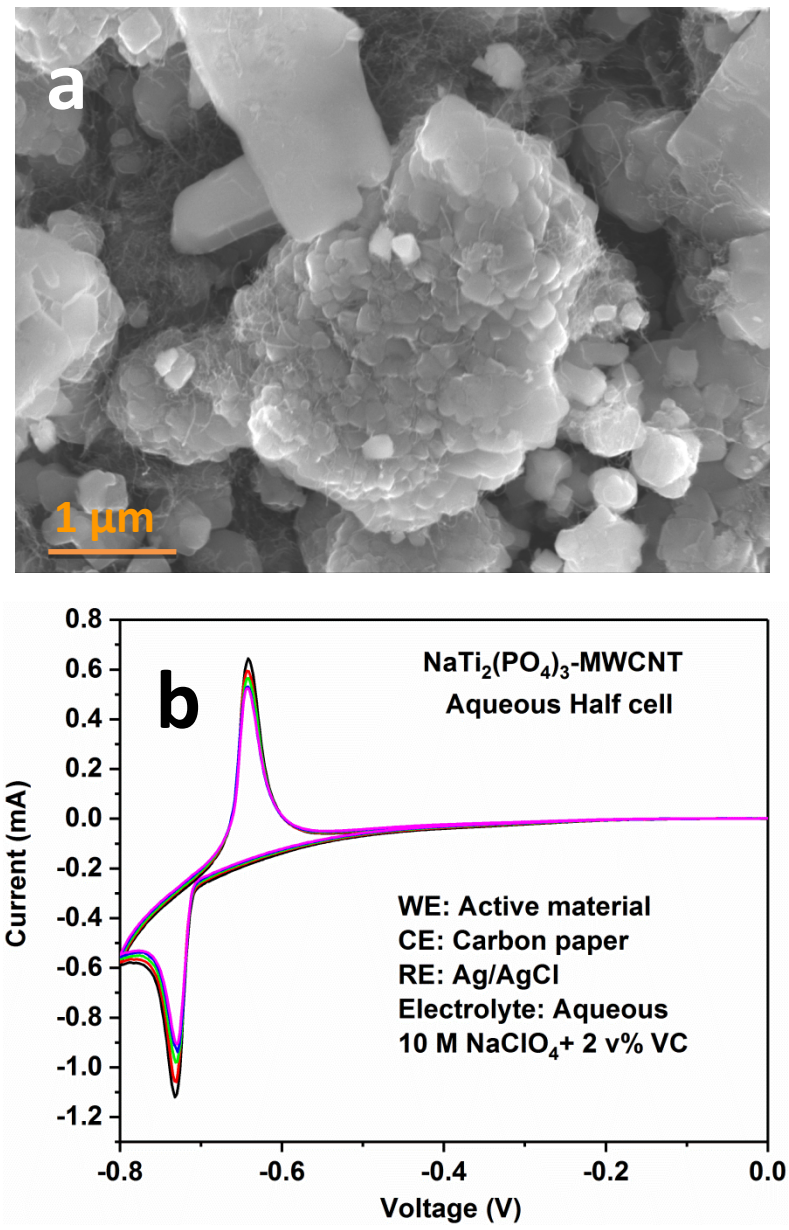

Figure S6: a) SEM image and b) Cyclic voltammetry plots in 10 M $NaClO_4$+2 v.% VC electrolyte for $NaTi_2(PO_4)_3$-MWCNT.